



Enhanced photocatalytic performance by the synergy of Bi vacancies and Bi⁰ in Bi⁰-Bi₂^δMoO₆

Lili Zhang^a, Zhiqiang Wang^c, Chun Hu^{a,b,*}, Baoyou Shi^a



^a Key Laboratory of Drinking Water Science and Technology, Research Center for Eco-Environmental Sciences, Chinese Academy of Sciences, Beijing, 100085, China

^b Institute of Environmental Research at Greater Bay, Key Laboratory for Water Quality and Conservation of the Pearl River Delta, Ministry of Education, Guangzhou University, Guangzhou, 510006, China

^c School of Environmental and Chemical Engineering, Tianjin Polytechnic University, Tianjin, 300387, China

ARTICLE INFO

Keywords:
Bi vacancies
Bi⁰
Strong interaction
Photocatalytic
Pollutants degradation

ABSTRACT

Bi vacancies and Bi⁰ containing Bi₂MoO₆ (Bi⁰-Bi₂^δMoO₆) was synthesized by a facile chemical reduction method. The visible-light-driven photoactivity of Bi₂MoO₆ was enhanced by nearly 7 times due to the synergy of Bi vacancies and Bi⁰. Based on the characterization of XRD, HRTEM, XRF, XPS, Raman, FTIR and PL, Bi vacancies and Bi⁰ coexisted in the crystal lattice of Bi₂MoO₆, and a strong interaction between Bi⁰ and Bi₂^δMoO₆ was observed. Bi vacancies were proved to enlarge the band gap to promote the separation of photogenerated electron-hole pairs, and Bi⁰ can act as an electron trap to accelerate the charge transfer by its strong interaction with Bi₂^δMoO₆, resulting in the high photoactivity of Bi⁰-Bi₂^δMoO₆ for the degradation of various organic pollutants under visible light. By the studies of ESR and other experiments, the charge transfer process was clarified that the fast separated electrons from Bi₂^δMoO₆ by Bi vacancies were transferred to Bi⁰ and further reacted to produce O₂^{·-}, and thus the photoexcited holes were accelerated to transfer to the surface of Bi₂^δMoO₆ to oxidize water into more ·OH and directly degrade organic pollutants in water.

1. Introduction

The use of abundant sunlight to split water into H₂ and O₂, reduce CO₂ and decompose harmful organic pollutants has been considered as one of the eco-friendly and energy-saving strategies [1–3]. For creation of efficient solar energy conversion systems, the development of visible-light photocatalysts has become one of the most important topics in photocatalysis research today. As an aurivillius oxide semiconductor, bismuth molybdate (Bi₂MoO₆) has recently emerged as a promising target for decomposing organic pollutants in waste water due to its non-toxicity, typical band gap (2.5–2.8 eV) and suitable CB/VB edge positions for visible light photocatalysis [4–6]. The practical application of Bi₂MoO₆ is limited by its poor quantum yield, which resulted from the rapid recombination of photoinduced charge carriers [7,8]. Thus, it is a challenge to modify Bi₂MoO₆ to improve photocatalytic activity.

Researchers have tried different strategies including morphology control [9–11], precious metal deposition [12], nonmetal or metal ion doping [13,14] and heterojunction construction [15,16]. Recently, a few reports have proved that engineering metal vacancies into photocatalysts is an effective method to enhance the photocatalytic activity for hydrogen production and water oxidation [17–19]. For instance,

Hao et al. has successfully introduced zinc vacancies into ZnS and discovered that appropriate amount of zinc vacancies remarkably improved the H₂ evolution under visible-light irradiation [17,18]. Di et al. has engineered bismuth vacancies into Bi₂WO₆ using BiOBr as template and found that bismuth vacancies favored water oxidation reactions [19]. Therefore, introducing Bi vacancies into Bi₂MoO₆ may be favorable for improving its photocatalytic activity.

On the other hand, a series of metal nanoparticles (NPs) such as Ag, Pt, Au, and Bi have been deposited on TiO₂ or ZnO to enhance the photoelectric or photocatalytic activities [20–23]. However, the normal mechanical mixing approach during synthesis resulted in unfavorable bad contact, which limited improving the efficiency of charge separation and transport. Therefore, direct growth of metal NPs dispersed on the semiconductor through an in-situ reduction reaction is highly desired. In previous reports, Bi/Bi₂MoO₆ hollow microspheres or porous NPs have been prepared by using glucose or ethylene glycol as reductive agents in microwave synthesis systems or MoO₃ as template [24,25]. This paper intends to simultaneously construct both Bi⁰ and Bi vacancies in Bi₂MoO₆ and investigate their roles in improving the photocatalytic performance of Bi₂MoO₆ under visible light.

In the present study, Bi vacancies and Bi⁰ containing Bi₂MoO₆ (Bi⁰-

* Corresponding author.

E-mail addresses: huchun@rcees.ac.cn, huchun@gzhu.edu.cn (C. Hu).

$\text{Bi}_{2-\delta}\text{MoO}_6$) was prepared with a chemical reduction method in aqueous solution under ambient condition. The simultaneous formation of Bi vacancies and Bi^0 was observed after reducing Bi_2MoO_6 with appropriate amount of NaBH_4 . $\text{Bi}-\text{Bi}_{2-\delta}\text{MoO}_6$ was found to be highly efficient to remove various pollutants in water. The enhanced photocatalytic efficiency was confirmed to come from the widened band gap by Bi vacancies for better charge separation, and the accelerated charge transfer by the strong interaction between Bi^0 and $\text{Bi}_{2-\delta}\text{MoO}_6$. The photocatalytic mechanism was discussed in detail.

2. Experimental

2.1. Preparation of catalysts

The pure Bi_2MoO_6 was prepared via a hydrothermal method. Typically, $\text{Bi}(\text{NO}_3)_3 \cdot 5\text{H}_2\text{O}$ was first dissolved in dilute acetic solution to get the final concentration 0.573 mol L^{-1} , and then dropwise added to the $\text{Na}_2\text{MoO}_4 \cdot 2\text{H}_2\text{O}$ (0.144 mol L^{-1}) aqueous solution. After being stirred for 30 min, the suspension was hydrothermally treated at 160°C for 2 h. After cooling down to room temperature, the resulting samples were filtered, washed and dried in vacuum at 60°C for 5 h to get pure Bi_2MoO_6 .

$\text{Bi}-\text{Bi}_{2-\delta}\text{MoO}_6$ was obtained by reducing pure Bi_2MoO_6 with NaBH_4 at room temperature. In a typical procedure, 0.5 g of pure Bi_2MoO_6 was dispersed in 50 mL of ultrapure water and stirred for 30 min. Different masses of NaBH_4 was added into the above solution. After being vigorously stirred for 6 h at room temperature, the solid product was collected by filtration, washed with ultrapure water and dried in vacuum at 60°C for 5 h. The obtained products were labeled as $\text{Bi}-\text{Bi}_{2-\delta}\text{MoO}_6\text{-R}$, where R was the molar ratio of NaBH_4 to 0.5 Bi_2MoO_6 .

2.2. Characterization

Powder X-ray diffraction (XRD) patterns were recorded on Scintag-XDS-2000 with $\text{Cu K}\alpha$ radiation ($\lambda = 1.540598 \text{ \AA}$) at 40 kV and 40 mA. The field-emission scanning electron microscopy (FESEM) images were taken on a SU8020 (Hitachi, Japan). The high-resolution transmission electron microscopy (HRTEM) images were obtained using a JEOL-2010 TEM operated at an acceleration voltage of 200 kV. The molar ratio of Bi/Mo in different samples was measured by X-ray fluorescence spectrometer (XRF, ARL PERFORM'X 4200). X-ray photoelectron spectroscopy (XPS) data were acquired on an AXIS-Ultra instrument from Kratos with an excitation source of monochromatic $\text{Al K}\alpha$ radiation (225 W, 15 mA, 15 kV). The C1 s peak at 284.8 eV was used to calibrate the binding energies. Raman measurements were carried out at room temperature in a Horiba LabRAM HR800 system with a CCD detector. The Raman signals were excited with a laser source at an excitation line of 532 nm. Fourier-transform infrared (FTIR) spectra were obtained using a Bruker Tensor 27 FTIR Spectrophotometer. The

photoluminescence (PL) spectra were taken on a FLS 980 luminescence spectrometer with an excitation wavelength of 350 nm. UV-vis diffuse reflectance spectra were recorded on a Shimadzu U3900 spectrophotometer using an integrating-sphere accessory. Electron spin resonance (ESR) spectra were obtained using a Bruker ESP 300E electron paramagnetic resonance spectrometer with BMPO as a spin adduct. Photoelectrochemical properties were evaluated using a CHI 660D electrochemical workstation in a conventional three-electrode cell with a saturated calomel electrode and as-prepared samples film electrodes on the indium-tin oxide (ITO) conducting glass as the reference and working electrodes, respectively. The photocurrent-time curves were measured under ambient conditions in $0.1 \text{ M Na}_2\text{SO}_4$ under visible light ($\lambda > 400 \text{ nm}$). The electrochemical impedance spectroscopy (EIS) was operated in the frequency range of 0.1 to 10^5 Hz in $0.1 \text{ M Na}_2\text{SO}_4$ solution. Mott-Schottky plots were recorded in a basic electrochemical system (AMETEK Princeton Applied Research, Oak Ridge, TN) with a two-compartment, three-electrode electrochemical cell.

2.3. Procedures and analysis

Photocatalytic activities of the as-prepared products were evaluated by examining the organic pollutants degradation under 150 W Xe arc lamp with a 400 nm cutoff filter as the visible light source. The incident light intensity was measured as 3.2 mW cm^{-2} by a radiometer from Photoelectric Instrument Factory Beijing Normal University. Typically, 0.1 g of catalyst was added into 60 mL of 10 mg L^{-1} organic pollutants aqueous solution. Before illumination, the suspension was placed in the dark under constant stirring for 30 min to ensure adsorption/desorption equilibrium. At certain time intervals, suspension samples were withdrawn. After removing the catalysts, the concentration decrease of organic substrate was measured using high-performance liquid chromatography (1200 series; Agilent) with a Zorbax SB-Aq column ($5 \mu\text{m}$, $4.6 \times 250 \text{ mm}$; Agilent) and UV detector. The total organic carbon (TOC) of the solution was analyzed using a TOC-V_{CPH} total carbon analyzer supplied by Shimadzu, Japan.

In addition, the possible leaching of metal ions during the reaction was monitored by inductively coupled plasma optical emission spectrometry (ICP-OES) on an Optima 2000 (PerkinElmer, Inc.) instrument. To test the recyclability of $\text{Bi}-\text{Bi}_{2-\delta}\text{MoO}_6$, the catalyst was filtered, washed with water, and dried at 60°C to be used in the next cycle. The above process was repeated five times.

The represented experimental data was the average of the triplicates with a standard deviation of less than 5%.

3. Results and discussion

3.1. Characterization of catalysts

The crystallographic structures of Bi_2MoO_6 and $\text{Bi}-\text{Bi}_{2-\delta}\text{MoO}_6$ were

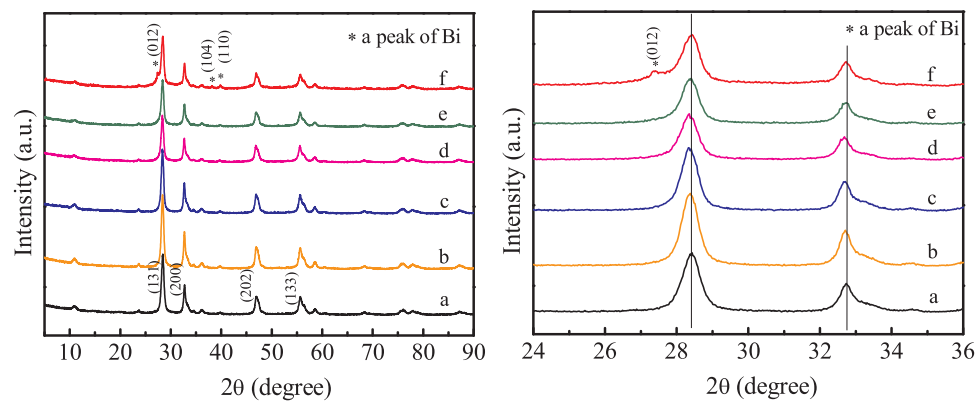


Fig. 1. XRD patterns (A) and the enlarged view (B) for pure Bi_2MoO_6 (a) and $\text{Bi}-\text{Bi}_{2-\delta}\text{MoO}_6\text{-R}$ ($R = 0.1$ (b), 0.2 (c), 0.3 (d), 0.4 (e), and 0.6 (f)).

characterized and shown in Fig. 1. The XRD pattern of the pure Bi_2MoO_6 was well indexed as orthorhombic Bi_2MoO_6 (JCPDS 21-0102), and no other impurity peak was observed. After reducing Bi_2MoO_6 , the dominant diffraction peaks of Bi_2MoO_6 shifted to lower angles. From the enlarged view in Fig. 1b, the largest shift was observed in $\text{Bi}-\text{Bi}_{2-\delta}\text{MoO}_{6-0.3}$, but the shift difference between $\text{Bi}-\text{Bi}_{2-\delta}\text{MoO}_{6-0.2}$ and $\text{Bi}-\text{Bi}_{2-\delta}\text{MoO}_{6-0.3}$ was subtle. Consistently, the interplanar distances of $\text{Bi}-\text{Bi}_{2-\delta}\text{MoO}_{6-0.2}$ (3.1443 \AA) and $\text{Bi}-\text{Bi}_{2-\delta}\text{MoO}_{6-0.3}$ (3.1446 \AA) were almost the same compared to the obviously larger differences of other samples (Table S1). With further increasing the amount of reductant during synthesis, the peak shift gradually decreased. And no obvious peak shift was found in $\text{Bi}-\text{Bi}_{2-\delta}\text{MoO}_{6-0.6}$, whilst the (012), (104), and (110) diffraction peaks of metallic Bi (JCPDS 44-1246) appeared. The crystal structure parameters in Table S1 showed that the peak shift toward lower angles indicated the increase of the interplanar distance and crystal size along with a decrease in strain. These changes after reduction could be attributed to the larger size of the reduced Bi in the lattice ($\text{Bi}^0 > \text{Bi}^+ > \text{Bi}^{3+}$) and the existence of Bi^0 in the interstitial sites [26]. The extraction of Bi ions from the cationic sites would result in the formation of Bi vacancies during the reduction process [27], which was further proved below. Moreover, the relatively larger peak shift for $\text{Bi}-\text{Bi}_{2-\delta}\text{MoO}_{6-0.2}$ and $\text{Bi}-\text{Bi}_{2-\delta}\text{MoO}_{6-0.3}$ suggested the coexistence of the more interstitial Bi^0 and Bi vacancies in the crystal lattice. The interstitial Bi^0 would be further out of the lattice to produce Bi NPs.

Based on quantitative results from XRF in Table S2, the atomic ratio of Bi and Mo in pure Bi_2MoO_6 was 1.94, while the value was 2.13 in $\text{Bi}-\text{Bi}_{2-\delta}\text{MoO}_{6-0.2}$, indicating the production of Bi^0 after reducing Bi_2MoO_6 . Accordingly, the yield of Bi^0 was 6.51 wt%. Theoretically, 6.51 wt% crystal Bi^0 can be found by XRD [28], however, no such diffraction peaks were found, indicating the existence of the interstitial Bi^0 and Bi clusters. The surface atom ratio of Bi to Mo gradually increased from pure Bi_2MoO_6 (2.61) to $\text{Bi}-\text{Bi}_{2-\delta}\text{MoO}_{6-0.6}$ (3.36) (Table S2), and light absorption in the range of 550–800 nm also gradually increased with their color changes from light yellow to grey (Fig. 6A), both indicating the increase of the amount of Bi NPs with increasing the amount of reductant during synthesis. In particular, compared to $\text{Bi}-\text{Bi}_{2-\delta}\text{MoO}_{6-0.2}$, the significantly increased surface Bi/Mo ratio and light absorption in 550–800 nm of $\text{Bi}-\text{Bi}_{2-\delta}\text{MoO}_{6-0.3}$ suggested the formation of more and larger Bi particles, which were proved to be not conducive to the photoactivities.

The existence of Bi^0 in $\text{Bi}-\text{Bi}_{2-\delta}\text{MoO}_{6-0.2}$ was further confirmed. As shown in Fig. 2A and B, both pure Bi_2MoO_6 and $\text{Bi}-\text{Bi}_{2-\delta}\text{MoO}_{6-0.2}$ presented two-dimensional (2D) nanoplates with particle size of 20–100 nm. TEM images of $\text{Bi}-\text{Bi}_{2-\delta}\text{MoO}_{6-0.2}$ exhibited the stack of nanoplates (Fig. 2C and D). The corresponding selected-area electron diffraction (SAED) pattern of Fig. 2C displayed the existence of (131), (200), (202) and (133) planes of orthorhombic Bi_2MoO_6 (the inset of Fig. 2C), which agreed well with the XRD result. A deeper inspection of Fig. 2D using HRTEM showed the presence of lattice fringes at 0.315 nm and 0.196 nm, which were according to the (131) and (202) d-spacing of Bi_2MoO_6 . Specially, the lattice fringes at 0.328 nm and 0.233 nm attributed to the d-spacing of (012) and (104) of Bi were observed, confirming the formation of trace amounts of Bi NPs on Bi_2MoO_6 for $\text{Bi}-\text{Bi}_{2-\delta}\text{MoO}_{6-0.2}$. Combined with the XRD and XRF results, Bi in $\text{Bi}-\text{Bi}_{2-\delta}\text{MoO}_{6-0.2}$ mainly existed as interstitial Bi^0 and Bi clusters.

The electronic structure and the surface composition were revealed by XPS analysis. The XPS survey spectra revealed that the tested samples were composed of Bi, Mo, O, and adventitious carbon (Fig. S1A). The C1 s peak at 284.8 eV was used to calibrate the binding energies (Fig. S1B). From the high-resolution Bi 4f XPS spectra of pure Bi_2MoO_6 , the two characteristic peaks located at 159.3 and 164.7 eV were attributed to $\text{Bi} 4f_{7/2}$ and $\text{Bi} 4f_{5/2}$ of Bi^{3+} [29]. These peaks in $\text{Bi}-\text{Bi}_{2-\delta}\text{MoO}_{6-0.2}$ were shifted down by 0.1 eV. Moreover, the peaks of Mo 3d at 232.6 and 235.7 eV, ascribing to $\text{Mo} 3d_{5/2}$ and $\text{Mo} 3d_{3/2}$ of Mo^{6+} in Bi_2MoO_6 [30], respectively, were also shifted down by about 0.1 eV in $\text{Bi}-\text{Bi}_{2-\delta}\text{MoO}_{6-0.2}$. The negative shift of both Bi 4f and Mo 3d in $\text{Bi}-\text{Bi}_{2-\delta}\text{MoO}_{6-0.2}$

suggested the partial reduction of Bi^{3+} and Mo^{6+} by NaBH_4 [31]. On the other hand, the increase of the surface electron density indicated the interaction between Bi^0 and $\text{Bi}-\text{Bi}_{2-\delta}\text{MoO}_{6-0.2}$ [32]. For $\text{Bi}-\text{Bi}_{2-\delta}\text{MoO}_{6-0.6}$, other two peaks at 156.9 and 162.3 eV attributed to the metallic Bi [33] and even the peak at 230.4 eV for Mo^{4+} appeared [34,35], indicating the formation of surface detectable Bi^0 due to the increased reduction level, which was consistent with the XRD result. In addition, the peaks of O 1s at about 530.0, 530.7, and 532.0 eV can be assigned to the lattice-oxygen (O_{lat}) including $\text{Bi}-\text{O}$ (O_{Bi}) and Mo-O (O_{Mo}), and the defect-oxygen (O_{def}) or surface hydroxyl-like group in pure Bi_2MoO_6 , respectively. From the XPS analysis in Table S2, the surface atom ratio of Bi to Mo for $\text{Bi}-\text{Bi}_{2-\delta}\text{MoO}_{6-0.2}$ (2.86) was higher than that for pure Bi_2MoO_6 (2.61), indicating the existence of surface Bi^0 . In contrast, the atom ratio of O_{Bi} to O_{Mo} for $\text{Bi}-\text{Bi}_{2-\delta}\text{MoO}_{6-0.2}$ (1.56) was much lower than that for pure Bi_2MoO_6 (2.04), while the ratio of O_{def} to O_{lat} was almost the same (0.075 for $\text{Bi}-\text{Bi}_{2-\delta}\text{MoO}_{6-0.2}$ and 0.071 for pure Bi_2MoO_6), suggesting that the formation of Bi vacancies rather than oxygen vacancies during the reducing process.

Raman peaks in the range of 600–900 and 200–400 cm^{-1} for pure Bi_2MoO_6 in Fig. S2 were ascribed to Mo-O stretching vibration bands and directly correlating Mo-O bond lengths of the distorted MoO_6 octahedra, respectively [36]. A strong band at 805 cm^{-1} corresponding to the stretching vibration and a peak at 143 cm^{-1} ascribing to the bending modes of MoO_6 octahedral unit in $\text{Bi}-\text{Bi}_{2-\delta}\text{MoO}_{6-0.2}$ were shifted compared to pure Bi_2MoO_6 , indicating the change in the chemical environment of $\text{Bi}-\text{Bi}_{2-\delta}\text{MoO}_{6-0.2}$ due to the interaction between Bi^0 and Bi_2MoO_6 or the existence of structure defects in Bi_2MoO_6 [37]. As shown in Fig. 4, the FTIR peaks at 729.4, 841.7 and 573.0 cm^{-1} were assigned to Mo-O, Mo-O-Mo bridging and Bi-O stretching modes, respectively. These peaks became weaker with increasing the amount of reductive agent during synthesis, indicating the existence of a strong interaction between Bi^0 and Bi_2MoO_6 in $\text{Bi}-\text{Bi}_{2-\delta}\text{MoO}_{6-0.2}$ [38]. In particular, the Bi-O band in $\text{Bi}-\text{Bi}_{2-\delta}\text{MoO}_{6-0.2}$ had a blue-shift from 573 cm^{-1} to 565 cm^{-1} . According to the classic vibration theory, the interface and space charges increased with the increase of metal vacancies, resulting in the movement of electric dipoles were less free, and thus the blue-shift of the metal-O band can be observed from FTIR spectra [39]. Herein, the blue-shift of the Bi-O band indicated that Bi vacancies were introduced into $\text{Bi}-\text{Bi}_{2-\delta}\text{MoO}_{6-0.2}$, in line with the XPS results. PL spectra can reflect structure defects in nano-sized semiconductor materials [40]. The increase of defects at surface generally produced higher photoluminescence intensity and photocatalytic activity [41]. As shown in Fig. 5, the PL intensity of $\text{Bi}-\text{Bi}_{2-\delta}\text{MoO}_{6-0.2}$ was significantly higher than that of pure Bi_2MoO_6 , indicating the increased structure defects in $\text{Bi}-\text{Bi}_{2-\delta}\text{MoO}_{6-0.2}$. Combining with the XPS and FTIR results, the increased structure defects were Bi vacancies. The excessive reduction would decrease the PL intensity for the reduced Bi vacancies in $\text{Bi}-\text{Bi}_{2-\delta}\text{MoO}_{6-0.2}$.

The optical properties of pure Bi_2MoO_6 and $\text{Bi}-\text{Bi}_{2-\delta}\text{MoO}_{6-0.2}$ were shown in Fig. 6. Bi_2MoO_6 absorbed sunlight with wavelengths less than 550 nm due to the intrinsic band gap transition. After reducing Bi_2MoO_6 , the absorption edge had a blue-shift, indicating the increase of the band gap energy. The band gap energies of the samples were estimated from the plots of $(ahv)^2$ versus the energy of absorbed light [13]. As shown in Fig. 6B, the E_g values were approximately 2.60 eV, 2.66 eV, 2.70 eV, 2.65 eV, and 2.62 eV for pure Bi_2MoO_6 , $\text{Bi}-\text{Bi}_{2-\delta}\text{MoO}_{6-0.1}$, $\text{Bi}-\text{Bi}_{2-\delta}\text{MoO}_{6-0.2}$, $\text{Bi}-\text{Bi}_{2-\delta}\text{MoO}_{6-0.3}$, and $\text{Bi}-\text{Bi}_{2-\delta}\text{MoO}_{6-0.4}$, respectively. The result suggested that the reduction can expand the band gap of Bi_2MoO_6 to enhance electron-hole separation. The band gap energy reached maximum in $\text{Bi}-\text{Bi}_{2-\delta}\text{MoO}_{6-0.2}$, however, overreduction could lower the band gap, surprisingly consistent with the shift of XRD peaks and the change of PL intensity. This result suggested the expansion of the band gap was mainly correlated with the formation of Bi vacancies as proved by XPS, FTIR and PL analysis.

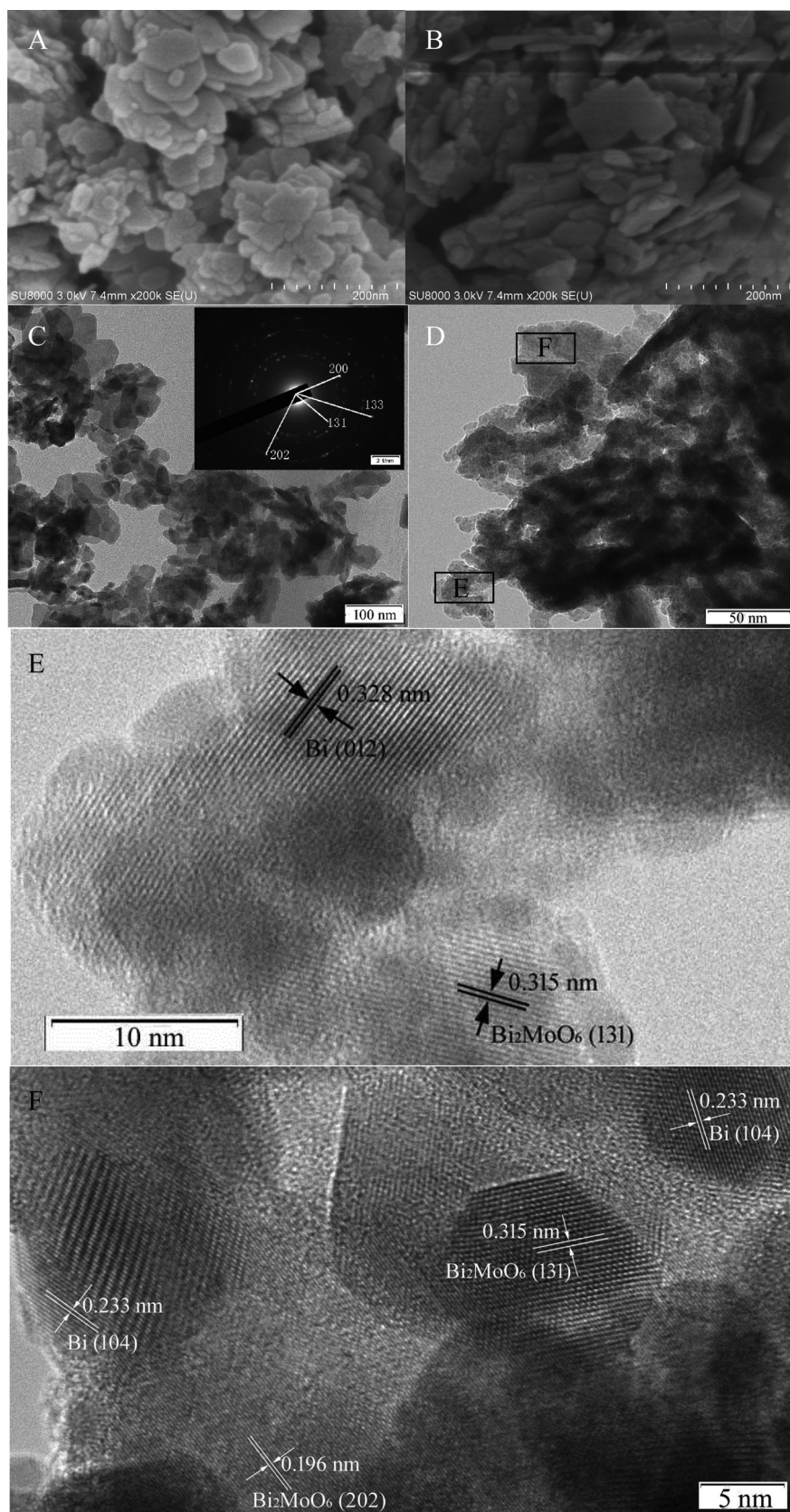


Fig. 2. FESEM images of pure Bi_2MoO_6 (A) and $\text{Bi}-\text{Bi}_2\delta\text{MoO}_6-0.2$ (B); TEM image (C and D) and HRTEM image (E and F) of $\text{Bi}-\text{Bi}_2\delta\text{MoO}_6-0.2$.

3.2. Photocatalytic performance

The photocatalytic performances of pure Bi_2MoO_6 and $\text{Bi}-\text{Bi}_2\delta\text{MoO}_6-0.2$

were tested under visible light irradiation ($\lambda > 400 \text{ nm}$, 3.2 mW cm^{-2}). As shown in Fig. 7, less than 28% of 2-CP was photodegraded after reaction for 180 min in pure Bi_2MoO_6 suspension. The

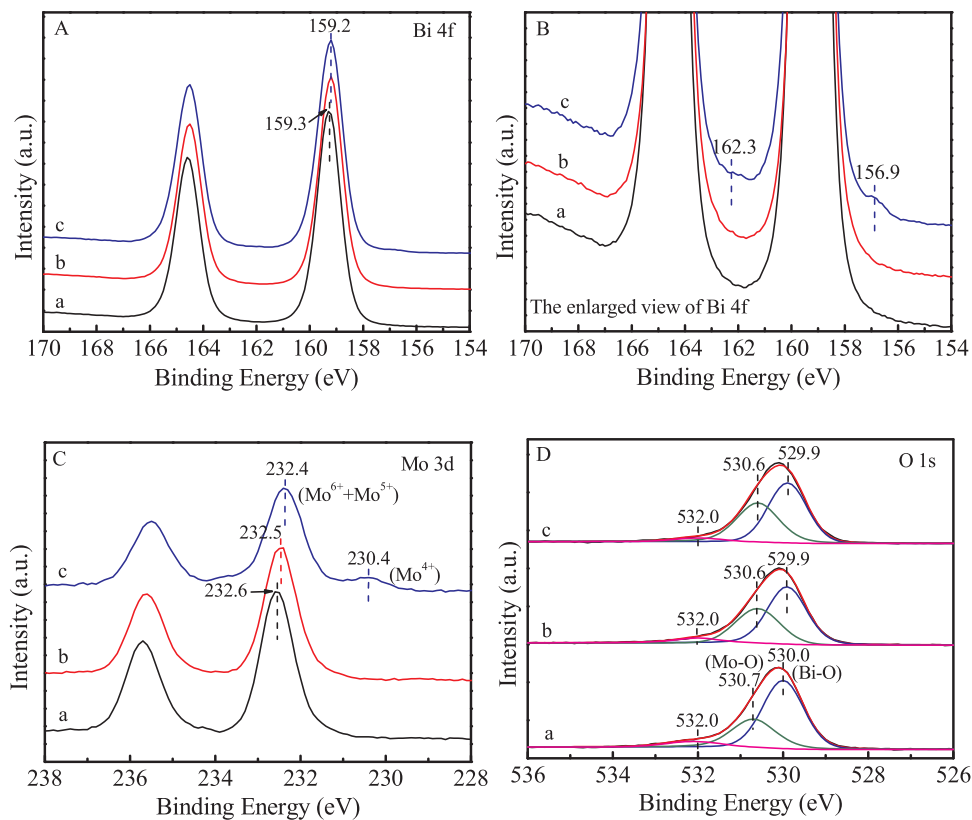


Fig. 3. XPS spectra of (a) pure Bi_2MoO_6 , (b) $\text{Bi}-\text{Bi}_{2-\delta}\text{MoO}_{6-0.2}$, and (c) $\text{Bi}-\text{Bi}_{2-\delta}\text{MoO}_{6-0.6}$: (A) Bi 4f, (B) the enlarged view of Bi 4f, (C) Mo 3d, and (D) O 1s.

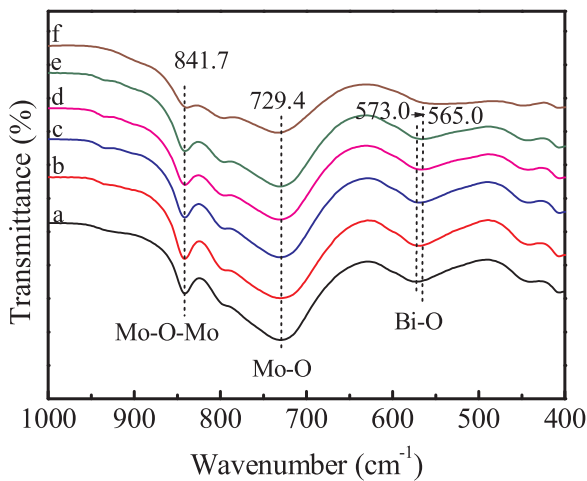


Fig. 4. FTIR spectra of (a) pure Bi_2MoO_6 , (b) $\text{Bi}-\text{Bi}_{2-\delta}\text{MoO}_{6-0.1}$, (c) $\text{Bi}-\text{Bi}_{2-\delta}\text{MoO}_{6-0.2}$, (d) $\text{Bi}-\text{Bi}_{2-\delta}\text{MoO}_{6-0.3}$, (e) $\text{Bi}-\text{Bi}_{2-\delta}\text{MoO}_{6-0.4}$, and (f) $\text{Bi}-\text{Bi}_{2-\delta}\text{MoO}_{6-0.6}$.

photodegradation of 2-CP was increased in $\text{Bi}-\text{Bi}_{2-\delta}\text{MoO}_6$ suspension. When increasing the molar ratio of $\text{NaBH}_4/0.5\text{Bi}_2\text{MoO}_6$ to 0.2 during synthesis, the photodegradation efficiency of 2-CP was significantly increased to 89% within 180 min under similar conditions. With further increasing the amount of reductant during synthesis, the photo-degradation of 2-CP was decreased. Accordingly, the highest TOC removal (61.69% within 180 min) was also achieved in $\text{Bi}-\text{Bi}_{2-\delta}\text{MoO}_{6-0.2}$ suspension. The change trends of the photocatalytic acitivity with the degree of reduction was in good agreement with the shift of the XRD diffraction peaks, the change of PL intensity and the band gap from UV-vis analysis, implying the relationship of structure and photocatalytic activity. The decrease of Bi vacancies and the growth of larger

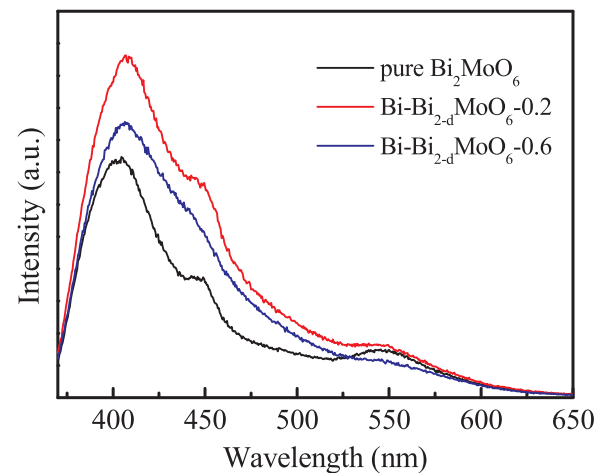


Fig. 5. Steady state photoluminescence over pure Bi_2MoO_6 , $\text{Bi}-\text{Bi}_{2-\delta}\text{MoO}_{6-0.2}$, and $\text{Bi}-\text{Bi}_{2-\delta}\text{MoO}_{6-0.6}$.

Bi particles would seriously lower its photocatalytic activity. To further compare the photocatalytic capacities of $\text{Bi}-\text{Bi}_{2-\delta}\text{MoO}_{6-0.2}$ and pure Bi_2MoO_6 , the kinetic constants were calculated. The reaction kinetics of all of the samples could be fitted well by the pseudo first order rate model with high correlation coefficients. The calculated k value for $\text{Bi}-\text{Bi}_{2-\delta}\text{MoO}_{6-0.2}$ was 0.73 h^{-1} , which was 6.8 times higher than that of pure Bi_2MoO_6 . In addition, during the photodegradation of 2-CP, no dissolved metal ions were detected in $\text{Bi}-\text{Bi}_{2-\delta}\text{MoO}_{6-0.2}$ suspension. And the cycle tests exhibited that 2-CP could be still degraded up to 80% within 180 min in the sixth cycle of $\text{Bi}-\text{Bi}_{2-\delta}\text{MoO}_{6-0.2}$ (Fig. S3). Furthermore, no phase change was observed in the XRD pattern of $\text{Bi}-\text{Bi}_{2-\delta}\text{MoO}_{6-0.2}$ after the 6th cycle reaction (Fig. S4). The results indicated that the catalyst was stable during photocatalytic reaction

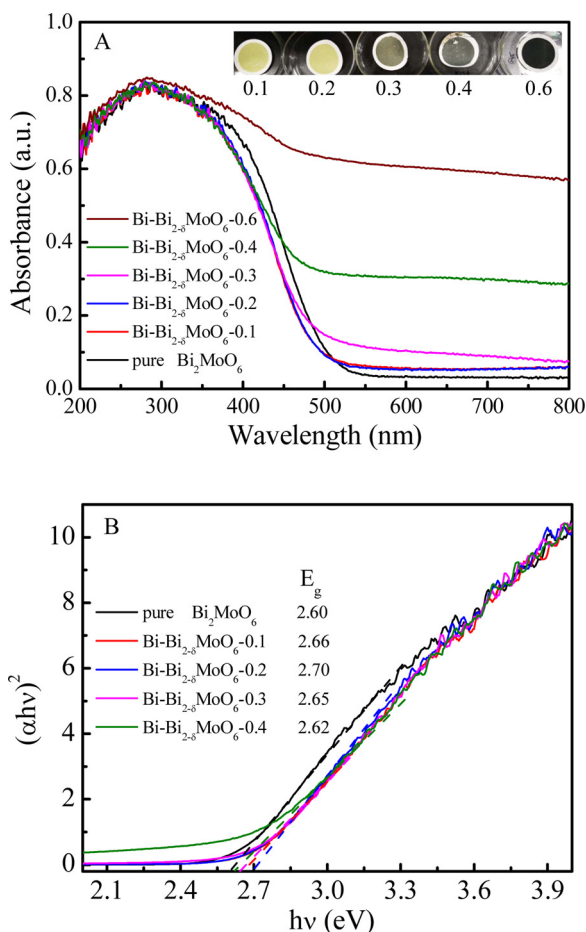


Fig. 6. UV-vis diffuse reflectance spectra with photos in the inset (A) and the corresponding Tauc's plots (B) of different samples.

under visible light. In addition, the elemental analysis result indicated the carbon element of the probable adsorbed species on the surface of fresh Bi-Bi₂_δMoO₆-0.2 and Bi-Bi₂_δMoO₆-0.2 after the 6th cycle reaction is 0.404 and 2.665%, respectively. Accordingly, the TOC residue on the surface of Bi-Bi₂_δMoO₆-0.2 after the cycle reaction is 2.261 mg L⁻¹. Therefore, the slight reduction in cycle performance of Bi-Bi₂_δMoO₆-0.2 was due to the inevitable surface TOC residue.

Bi-Bi₂_δMoO₆-0.2 was also highly effective for photocatalytic degradation of RhB, BPA, SMZ and phenol under visible light. As shown in Fig. 8, RhB can be completely decolorized within 90 min, and BPA can be completely degraded within 150 min. The corresponding TOC removal of RhB and BPA was up to 65.7% and 62.5% within 180 min, respectively. Moreover, the refractory SMZ and phenol could be degraded 72.2% and 33.9% with 35.5% and 26.0% of the TOC removal rate within 180 min, respectively.

The transient photocurrent responses were recorded via several on-off cycles of visible light irradiation to give evidence for the photoactivity of Bi-Bi₂_δMoO₆-0.2. As shown in Fig. 9A, the photocurrent of Bi-Bi₂_δMoO₆-0.2 was significantly enhanced compared to pure Bi₂MoO₆, indicating the highly efficient charge separation and transfer in Bi-Bi₂_δMoO₆-0.2. The EIS Nyquist plots of the samples were further measured and compared to reflect the reaction rate at the surface of catalysts as shown in Fig. 9B. Obviously, Bi-Bi₂_δMoO₆-0.2 had a smaller arc radius with respect to Bi₂MoO₆, indicating its faster interfacial charge transfer than that of Bi₂MoO₆. Therefore, the high activity and stability of Bi-Bi₂_δMoO₆-0.2 were probably related to the production of Bi vacancies and Bi⁰ after reduction. The Bi vacancies could enlarge the band gap to promote electron-hole separation, and the close contact between Bi₂_δMoO₆ and Bi⁰ could facilitate the charge transfer

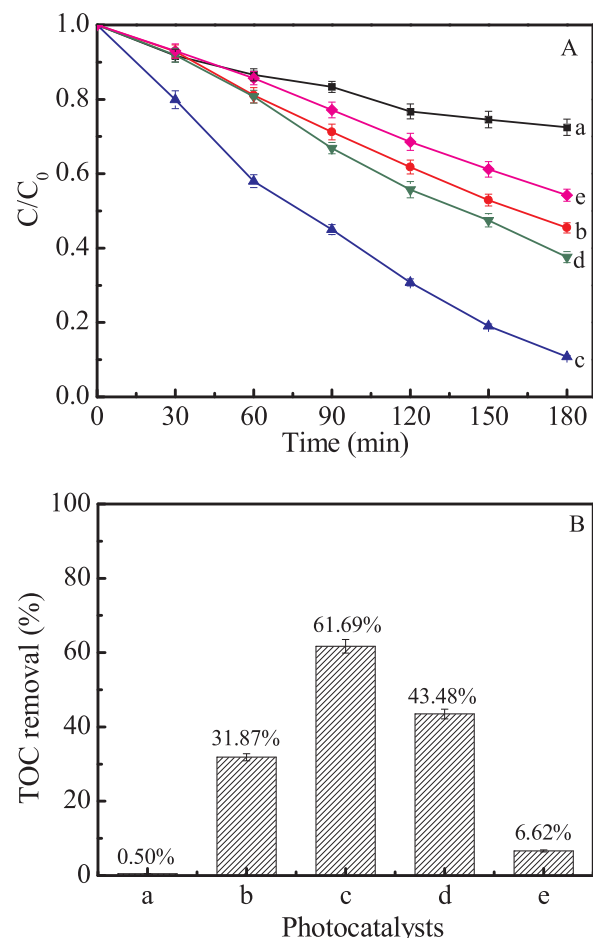


Fig. 7. Photodegradation of 2-CP (10 mg L⁻¹) (A) and the corresponding TOC removal (B) under visible light ($\lambda > 400$ nm) in different suspensions (1.6 g L⁻¹): (a) pure Bi₂MoO₆, (b) Bi-Bi₂_δMoO₆-0.1, (c) Bi-Bi₂_δMoO₆-0.2, (d) Bi-Bi₂_δMoO₆-0.3, and (e) Bi-Bi₂_δMoO₆-0.4.

more efficiently.

3.3. Photocatalytic mechanism

To identify the primary reactive species involved in removing organic pollutants over Bi-Bi₂_δMoO₆-0.2 under visible light, the effects of various radical scavengers on the degradation of 2-CP were examined in Fig. S5. The addition of h⁺ scavenger disodium ethylenediaminetetraacetate (EDTA-2Na) and superoxide (O₂^{·-}) scavenger p-benzoquinone strongly inhibited the degradation of 2-CP and only about 30% of 2-CP were degraded in Bi-Bi₂_δMoO₆-0.2 suspension under visible light ($\lambda > 400$ nm) after 180 min. Moreover, the degradation rate of 2-CP was changed with the addition of hydroxyl radicals (·OH) scavenger t-butanol. Furthermore, the BMPO spin-trapping ESR technique was used to detect the production of ·OH (Fig. 10). No significant characteristic peaks of BMPO-·OH were observed for pure Bi₂MoO₆ and the reduced samples in dark. Under visible light irradiation, only Bi-Bi₂_δMoO₆-0.1 and Bi-Bi₂_δMoO₆-0.2 showed obvious characteristic peaks of BMPO-·OH, and the peaks in Bi-Bi₂_δMoO₆-0.2 suspension were a little higher than Bi-Bi₂_δMoO₆-0.1, indicating the production of more ·OH radicals after illuminating Bi-Bi₂_δMoO₆-0.2. Combined with the structure characterization, the Bi vacancies and interstitial Bi⁰, which have been proved to promote electron-hole separation and facilitate charge transfer, respectively, were responsible for the photogeneration of more ·OH in Bi-Bi₂_δMoO₆-0.2, while the growth of larger Bi particles would be not conducive to the ·OH production, in agreement with the photoactivities of different samples.

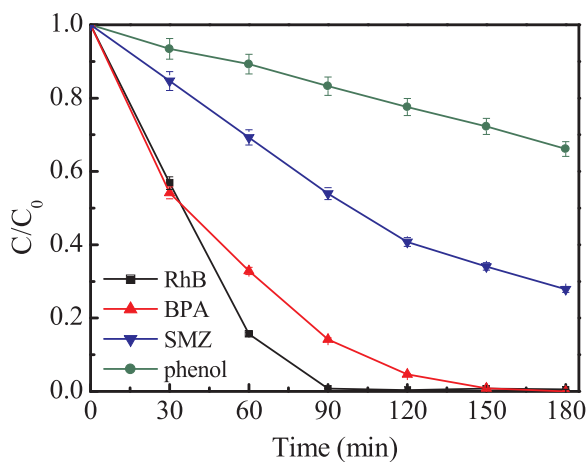


Fig. 8. Photodegradation of different pollutants (10 mg L^{-1}) in $\text{Bi-Bi}_2\text{MoO}_6\text{-}0.2$ (1.6 g L^{-1}) suspensions under visible light ($\lambda > 400 \text{ nm}$).

To better explain the production of active species and clarify the charge transport processes, the band structures were investigated. The band positions of pure Bi_2MoO_6 were calculated by the following formula: $E_{VB} = \chi - E^e + 0.5 E_g$ and $E_{CB} = E_{VB} - E_g$, where E_{VB} and E_{CB} are the valence band (VB) edge potential and the conduction band (CB) edge potential, χ is the absolute electronegativity of the semiconductor (5.55 for Bi_2MoO_6) [42], E^e is the energy of free electrons on hydrogen scale (4.5 eV), and E_g is the band gap energy. Correspondingly, the CB and VB edge potentials of Bi_2MoO_6 are -0.25 eV and 2.35 eV, respectively. From the VB-XPS spectra, the position of the Fermi level of semiconductors with respect to the valence band maximum (VBM) could be determined by extrapolating the leading edge of the VB to its intersection with background counts near the Fermi level [29]. As shown in Fig. S6, the value for both pure Bi_2MoO_6 and $\text{Bi-Bi}_2\delta\text{MoO}_6\text{-}0.2$ was 2.18. From the XPS analysis in Fig. 3, the Fermi level of $\text{Bi}_2\delta\text{MoO}_6$ with Bi vacancies was more negative than that of pure Bi_2MoO_6 , due to the whole negative shift of the binding energies of Bi, Mo and O atoms. Thus, the corresponding VB position of $\text{Bi}_2\delta\text{MoO}_6$ was estimated to be relatively more negative than that of pure Bi_2MoO_6 . In addition, the flat potential of $\text{Bi-Bi}_2\delta\text{MoO}_6\text{-}0.2$ was also more negative by about 0.10 eV compared to pure Bi_2MoO_6 (Fig. S7), indicating the more negative CB position of $\text{Bi}_2\delta\text{MoO}_6$. Therefore, the band structures of Bi_2MoO_6 before and after reduction can be relatively compared in Fig. S8. Generally, the holes generated on the more negative VB position possess weaker oxidizing ability from the view of the thermodynamics aspect. However, $\cdot\text{OH}$ radicals were produced in $\text{Bi-Bi}_2\delta\text{MoO}_6\text{-}0.2$ suspension but not in pure Bi_2MoO_6 suspension as confirmed by ESR

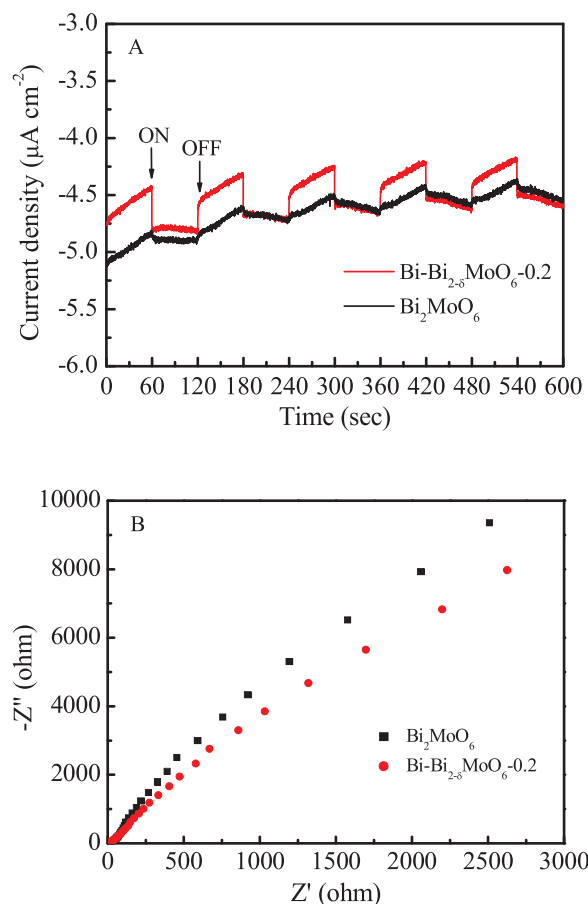


Fig. 9. Transient photocurrent responses (A) and EIS Nyquist plots (B) of Bi_2MoO_6 and $\text{Bi-Bi}_2\delta\text{MoO}_6\text{-}0.2$ under visible light ($\lambda > 400 \text{ nm}$).

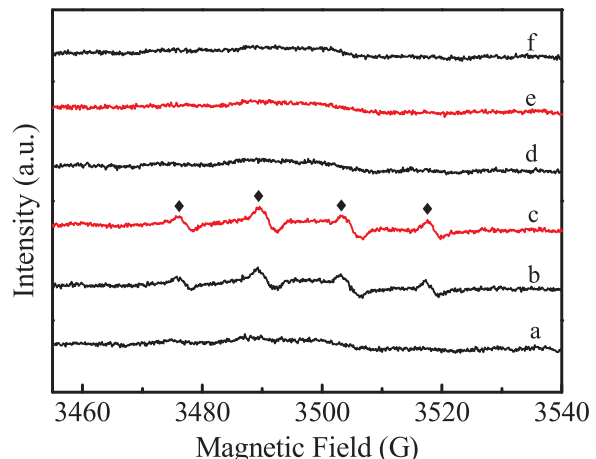
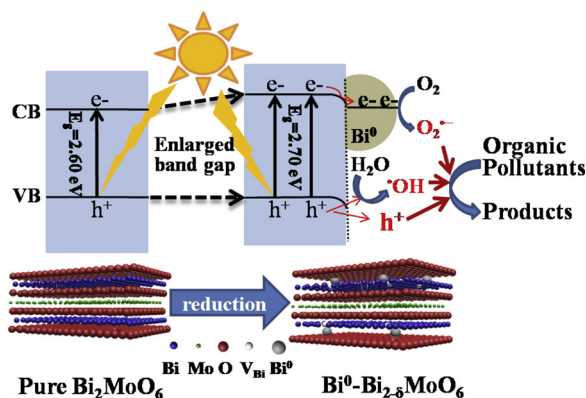


Fig. 10. BMPO spin-trapping ESR spectra recorded for $\text{BMPO}\cdot\text{OH}$ under visible light ($\lambda > 400 \text{ nm}$) in aqueous dispersion of pure Bi_2MoO_6 (a) and $\text{Bi-Bi}_2\delta\text{MoO}_6\text{-}R$ ($R = 0.1$ (b), 0.2 (c), 0.3 (d), 0.4 (e), and 0.6 (f)).

analysis, implying that the kinetic factors played more important roles in this system. The faster charge separation and transfer in the $\text{Bi-Bi}_2\delta\text{MoO}_6\text{-}0.2$ system would result in the photogeneration of more holes to oxidize water into more $\cdot\text{OH}$. As the Fermi level of $\text{Bi}_2\delta\text{MoO}_6$ is lower than that of Bi (-0.17 eV) [43], the close contact between $\text{Bi}_2\delta\text{MoO}_6$ and Bi^0 would promote the electron transfer from Bi to $\text{Bi}_2\delta\text{MoO}_6$ until their Fermi levels were aligned. Under equilibrium, the Bi^0 was positively charged and the semiconductor $\text{Bi}_2\delta\text{MoO}_6$ was negatively charged near the interface due to electrostatic induction as shown in



Scheme 1. Proposed photocatalytic mechanism for Bi-Bi_{2.8}MoO₆-0.2.

Fig. S9 [44]. In this region, the energy band edges in Bi_{2.8}MoO₆ bended downward toward the interface due to the electric field between Bi_{2.8}MoO₆ and Bi⁰, forming the ohmic contact. After the illumination of visible light, the ohmic contact facilitated a quick transfer of electrons from negatively charged Bi_{2.8}MoO₆ to the positively charged Bi⁰, while the holes would keep in the VB of Bi_{2.8}MoO₆. The surface plasmon resonance (SPR) absorption of Bi⁰ was found to be centered around 500 nm or 550 nm by several groups [25,33]. In order to determine whether the SPR of Bi⁰ worked in the Bi-Bi_{2.8}MoO₆-0.2 system, the photoactivities of Bi₂MoO₆ and Bi-Bi_{2.8}MoO₆-0.2 were tested under monochromatic light ($\lambda = 535$ nm). As shown in Fig. S10, no photo-degradation of 2-CP was found, indicating no SPR of Bi⁰ worked for the removal of pollutants in the Bi-Bi_{2.8}MoO₆-0.2 system. Therefore, as shown in Scheme 1, the photogenerated electron-hole pairs were able to be rapidly separated by the enlarged band gap by Bi vacancies, and effectively transported by the strong interaction between Bi_{2.8}MoO₆ and Bi⁰, resulting in the generation of more holes to oxidize water into more ·OH or directly degrade organic pollutants.

4. Conclusions

The Bi-Bi_{2.8}MoO₆ was successfully prepared by a facile chemical reduction method with the production of Bi vacancies and Bi⁰. The visible-light-driven photoactivity of Bi-Bi_{2.8}MoO₆-0.2 was 6.8 times higher than that of pure Bi₂MoO₆. The characterization results showed the existence of Bi vacancies and Bi⁰ in Bi₂MoO₆ after reduction and a strong interaction between Bi⁰ and Bi_{2.8}MoO₆. It was confirmed that Bi vacancies could enlarge the band gap for efficient charge separation. The strong interaction between Bi⁰ and Bi_{2.8}MoO₆ promoted electrons transfer from Bi_{2.8}MoO₆ to Bi⁰, and the photogenerated holes concentrated on Bi_{2.8}MoO₆ rapidly converted surface adsorbed water into highly oxidizing ·OH and directly reacted with pollutants, leading to the fast and stable degradation and mineralization of various organic pollutants under visible light. This work highlights the synergistic function of Bi vacancies and Bi⁰, and provides a simple strategy for developing highly effective photocatalysts for water purification under visible light.

Acknowledgments

This work was supported by National Key Research and Development Plan (2016YFA0203200), the National Natural Science Foundation of China (Grant Nos. 51538013, 51838005), and Open Project Program of Key Laboratory for Water Quality and Conservation of the Pearl River Delta, Ministry of Education of China, Guangzhou University (0601GD001).

Appendix A. Supplementary data

Supplementary material related to this article can be found, in the online version, at doi:<https://doi.org/10.1016/j.apcatb.2019.117785>.

References

- [1] H. Wang, S. Jiang, W. Shao, X. Zhang, S. Chen, X. Sun, Q. Zhang, Y. Luo, Y. Xie, Optically switchable photocatalysis in ultrathin black phosphorus nanosheets, *J. Am. Chem. Soc.* 140 (2018) 3474–3480.
- [2] Y. Feng, H. Li, L. Ling, S. Yan, D. Pan, H. Ge, H. Li, Z. Bian, Enhanced photocatalytic degradation performance by fluid-induced piezoelectric field, *Environ. Sci. Technol.* 52 (2018) 7842–7848.
- [3] H. Dong, X. Guo, C. Yang, Z. Ouyang, Synthesis of g-C₃N₄ by different precursors under burning explosion effect and its photocatalytic degradation for tylosin, *Appl. Catal. B: Environ.* 230 (2018) 65–76.
- [4] J. Tian, P. Hao, N. Wei, H. Cui, H. Liu, 3D Bi₂MoO₆ nanosheet/TiO₂ nanobelts heterostructure: enhanced photocatalytic activities and photoelectrochemistry performance, *ACS Catal.* 5 (2015) 4530–4536.
- [5] J. Li, Y. Yin, E. Liu, Y. Ma, J. Wan, J. Fan, X. Hu, In situ growing Bi₂MoO₆ on g-C₃N₄ nanosheets with enhanced photocatalytic hydrogen evolution and disinfection of bacteria under visible light irradiation, *J. Hazard. Mater.* 321 (2017) 183–192.
- [6] J. Liang, F. Liu, J. Deng, M. Li, M. Tong, Efficient bacterial inactivation with Z-scheme AgI/Bi₂MoO₆ under visible light irradiation, *Water Res.* 123 (2017) 632–641.
- [7] Y. Sun, J. Wu, T. Ma, P. Wang, C. Cui, D. Ma, Synthesis of C@Bi₂MoO₆ nanocomposites with enhanced visible light photocatalytic activity, *Appl. Surf. Sci.* 403 (2017) 141–150.
- [8] X. Meng, Z. Zhang, Plasmonic ternary Ag-rGO-Bi₂MoO₆ composites with enhanced visible-light-driven photocatalytic activity, *J. Catal.* 344 (2016) 616–630.
- [9] M. Wu, Y. Wang, Y. Xu, J. Ming, M. Zhou, R. Xu, Q. Fu, Y. Lei, Self-supported Bi₂MoO₆ nanowall for photoelectrochemical water splitting, *ACS Appl. Mater. Interfaces* 9 (2017) 23647–23653.
- [10] T. Yu, Z. Li, S. Chen, Y. Ding, W. Chen, X. Liu, Y. Huang, F. Kong, Facile synthesis of flowerlike Bi₂MoO₆ hollow microspheres for high-performance supercapacitors, *ACS Sustain. Chem. Eng.* 6 (2018) 7355–7361.
- [11] Y. Ma, Y. Jia, Z. Jiao, M. Yang, Y. Qi, Y. Bi, Hierarchical Bi₂MoO₆ nanosheet-built frameworks with excellent photocatalytic properties, *Chem. Commun.* 51 (2015) 6655–6658.
- [12] D. Wang, H. Shen, L. Guo, C. Wang, F. Fua, Y. Liang, Ag/Bi₂MoO_{6-x} with enhanced visible-light-responsive photocatalytic activities via the synergistic effect of surface oxygen vacancies and surface plasmon, *Appl. Surf. Sci.* 436 (2018) 536–547.
- [13] C. Yu, Z. Wu, R. Liu, D.D. Dionysiou, K. Yang, C. Wang, H. Liu, Novel fluorinated Bi₂MoO₆ nanocrystals for efficient photocatalytic removal of water organic pollutants under different light source illumination, *Appl. Catal. B: Environ.* 209 (2017) 1–11.
- [14] Z. Dai, F. Qin, H. Zhao, J. Ding, Y. Liu, R. Chen, Crystal defect engineering of aurivillius Bi₂MoO₆ by Ce doping for increased reactive species production in photocatalysis, *ACS Catal.* 6 (2016) 3180–3192.
- [15] J. Zhang, C. Shao, X. Li, J. Xin, R. Tao, Y. Liu, Assembling n-Bi₂MoO₆ nanosheets on electrospun p-CuAl₂O₄ hollow nanofibers: enhanced photocatalytic activity based on highly efficient charge separation and transfer, *ACS Sustain. Chem. Eng.* 6 (2018) 10714–10723.
- [16] B. Jin, Z. Jiao, Y. Bi, Efficient charge separation between Bi₂MoO₆ nanosheets and ZnO nanowires for enhanced photoelectrochemical properties, *J. Mater. Chem. A* 3 (2015) 19702–19705.
- [17] X. Hao, Y. Wang, J. Zhou, Z. Cui, Y. Wang, Z. Zou, Zinc vacancy-promoted photocatalytic activity and photostability of ZnS for efficient visible-light-driven hydrogen evolution, *Appl. Catal. B: Environ.* 221 (2018) 302–311.
- [18] X. Hao, J. Zhou, Z. Cui, Y. Wang, Y. Wang, Z. Zou, Zn-vacancy mediated electron-hole separation in ZnS/g-C₃N₄ heterojunction for efficient visible-light photocatalytic hydrogen production, *Appl. Catal. B: Environ.* 229 (2018) 41–51.
- [19] J. Di, C. Chen, C. Zhu, M. Ji, J. Xia, C. Yan, W. Hao, S. Li, H. Li, Z. Liu, Bismuth vacancy mediated single unit cell Bi₂WO₆ nanosheets for boosting photocatalytic oxygen evolution, *Appl. Catal. B: Environ.* 238 (2018) 119–125.
- [20] M.G. Méndez-Medrano, E. Kowalska, A. Lehoux, A. Herissan, B. Ohtani, D. Bahena, V. Brioso, C. Colbeau-Justin, J.L. Rodríguez-López, H. Remita, Surface modification of TiO₂ with Ag nanoparticles and CuO nanoclusters for application in photocatalysis, *J. Phys. Chem. C* 120 (2016) 5143–5154.
- [21] Y. Zhang, J. Zhou, Z. Li, Q. Feng, Photodegradation pathway of Rhodamine B with novel Au nanorods@ZnO microspheres driven by visible light irradiation, *J. Mater. Sci.* 53 (2018) 3149–3162.
- [22] S. Bharadwaja, A. Pandeya, B. Yagci, V. Ozguza, A. Qureshia, Graphene nano-mesh-Ag-ZnO hybrid paper for sensitive SERS sensing and self-cleaning of organic pollutants, *Chem. Eng. J.* 336 (2018) 445–455.
- [23] W. Wang, D. Zhu, Z. Shen, J. Peng, J. Luo, X. Liu, One-pot hydrothermal route to synthesize the Bi-doped anatase TiO₂ hollow thin sheets with prior facet exposed for enhanced visible-light-driven photocatalytic activity, *Ind. Eng. Chem. Res.* 55 (2016) 6373–6383.
- [24] J. Li, X. Liu, L. Pan, W. Qina, Z. Sun, Enhanced visible light photocatalytic degradation of Rhodamine B by Bi/Bi₂MoO₆ hollow microsphere composites, *RSC Adv.* 4 (2014) 62387–62392.
- [25] Y. Ma, Y. Jia, L. Wang, M. Yang, Y. Bi, Y. Qi, Efficient charge separation between Bi and Bi₂MoO₆ for photoelectrochemical properties, *Chem. Eur. J.* 22 (2016)

5844–5848.

[26] A.M. Saroja, I.K. Punithavathy, S.J. Jeyakumar, A.R. Balu, S.J. Gnanamuthu, Effect of Co doping on the physical properties of Sn_2S_3 thin film, *J. Mater. Sci. Mater. Electron.* 28 (2017) 11464–11472.

[27] C. Zhan, Z. Yao, J. Lu, L. Ma, V.A. Maroni, L. Li, E. Lee, E.E. Alp, T. Wu, J. Wen, Y. Ren, C. Johnson, M.M. Thackeray, M.K.Y. Chan, C. Wolverton, K. Amine Enabling the high capacity of lithium-rich antifluorite lithium iron oxide by simultaneous anionic and cationic redox, *Nat. Energy* 2 (2017) 963–971.

[28] K. Wang, Y. Li, G. Zhang, J. Li, X. Wu, 0D Bi nanodots/2D Bi_2NbO_7 nanosheets heterojunctions for efficient visible light photocatalytic degradation of antibiotics: enhanced molecular oxygen activation and mechanism insight, *Appl. Catal. B: Environ.* 240 (2019) 39–49.

[29] L. Zhang, C. Hu, H. Ji, p-Agl anchored on {001} facets of n- $\text{Bi}_2\text{O}_2\text{CO}_3$ sheets with enhanced photocatalytic activity and stability, *Appl. Catal. B: Environ.* 205 (2017) 34–41.

[30] C. Guan, W. Xiao, H. Wu, X. Liu, W. Zang, H. Zhang, J. Ding, Y. Feng, S.J. Pennycook, J. Wang, Hollow Mo-doped CoP nanoarrays for efficient overall water splitting, *Nano Energy* 48 (2018) 73–80.

[31] W. He, Y. Sun, G. Jiang, H. Huang, X. Zhang, F. Dong, Activation of amorphous Bi_2WO_6 with synchronous Bi metal and Bi_2O_3 coupling: photocatalysis mechanism and reaction pathway, *Appl. Catal. B: Environ.* 232 (2018) 340–347.

[32] Y. Gao, Y. Huang, Y. Li, Q. Zhang, J. Cao, W. Ho, S. Lee, Plasmonic Bi/ZnWO₄ microspheres with improved photocatalytic activity on NO removal under visible light, *ACS Sustain. Chem. Eng.* 4 (2016) 6912–6920.

[33] Z. Zhao, W. Zhang, Y. Sun, J. Yu, Y. Zhang, H. Wang, F. Dong, Z. Wu, Bi cocatalyst/ Bi_2MoO_6 microspheres nanohybrid with SPR-promoted visible-light photocatalysis, *J. Phys. Chem. C* 120 (2016) 11889–11898.

[34] A. Santoni, F. Rondino, C. Malerba, M. Valentini, A. Mittiga, Electronic structure of Ar⁺ ion-sputtered thin-film MoS₂: a XPS and IPES study, *Appl. Surf. Sci.* 392 (2017) 795–800.

[35] J. Dong, Y. Shi, C. Huang, Q. Wu, T. Zeng, W. Yao, A new and stable Mo-Mo₂C modified g-C₃N₄ photocatalyst for efficient visible light photocatalytic H₂ production, *Appl. Catal. B: Environ.* 243 (2019) 27–35.

[36] J. Ke, X. Duan, S. Luo, H. Zhang, H. Sun, J. Liu, M. Tade, S. Wang, UV-assisted construction of 3D hierarchical rGO/ Bi_2MoO_6 composites for enhanced photocatalytic water oxidation, *Chem. Eng. J.* 313 (2017) 1447–1453.

[37] Z. Dai, F. Qin, H. Zhao, F. Tian, Y. Liu, R. Chen, Time-dependent evolution of the $\text{Bi}_{3.64}\text{Mo}_{0.36}\text{O}_{6.55}/\text{Bi}_2\text{MoO}_6$ heterostructure for enhanced photocatalytic activity via the interfacial hole migration, *Nanoscale* 7 (2015) 11991–11999.

[38] Y. Huang, S. Kang, Y. Yang, H. Qina, Z. Ni, S. Yang, X. Li, Facile synthesis of Bi/ Bi_2WO_6 nanocomposite with enhanced photocatalytic activity under visible light, *Appl. Catal. B: Environ.* 196 (2016) 89–99.

[39] X. Sun, J. Wu, Q. Li, Q. Liu, Y. Qi, L. You, Z. Ji, P. He, P. Sheng, J. Ren, W. Zhang, J. Lu, J. Zhang, Fabrication of BioIO₃ with induced oxygen vacancies for efficient separation of the electron-hole pairs, *Appl. Catal. B: Environ.* 218 (2017) 80–90.

[40] L. Jing, Y. Qu, B. Wang, S. Li, B. Jiang, L. Yang, W. Fu, H. Fu, J. Sun, Review of photoluminescence performance of nano-sized semiconductor materials and its relationships with photocatalytic activity, *Sol. Energy Mater. Sol. Cells* 90 (2006) 1773–1787.

[41] M. Shaban, A.M. Ashraf, M.R. Abukhadra, TiO₂ nanoribbons/carbon nanotubes composite with enhanced photocatalytic activity: fabrication, characterization, and application, *Sci. Rep.* 8 (2018) 781–798.

[42] H. Li, J. Liu, W. Hou, N. Du, R. Zhang, X. Tao, Synthesis and characterization of g-C₃N₄/ Bi_2MoO_6 heterojunctions with enhanced visible light photocatalytic activity, *Appl. Catal. B: Environ.* 160–161 (2014) 89–97.

[43] F. Dong, Z. Zhao, Y. Sun, Y. Zhang, S. Yan, Z. Wu, An advanced semimetal–organic Bi spheres–g-C₃N₄ nanohybrid with SPR-enhanced visible-light photocatalytic performance for NO purification, *Environ. Sci. Technol.* 49 (2015) 12432–12440.

[44] Z. Zhang, J.T. Yates, Band bending in semiconductors: chemical and physical consequences at surfaces and interfaces, *Chem. Rev.* 112 (2012) 5520–5551.